Investigation of residual stresses and modeling of tensile deformation in wire-arc additive manufactured 6061 aluminum alloy: Diffraction and elastoplastic self-consistent model

Gautier Doumenc, Bruno Courant, Laurent Couturier, Pascal Paillard, Baptiste Girault, Thilo Pirling, Sandra Cabeza, M.-J. Moya, David Gloaguen

Investigation of residual stresses and modeling of tensile deformation in wire-arc additive manufactured 6061 aluminum alloy: diffraction and elastoplastic self-consistent model

Gautier Doumenc[1,2,3], Bruno Courant[3], Laurent Couturier[2], Pascal Paillard[2], Baptiste Girault[3], Thilo Pirling[4], Sandra Cabeza[4], M-J. Moya[3], David Gloaguen[3]

1: IRT Jules Verne, Technocampus Composite, Chemin du Chaffault, 44340 Bouguenais, France.
2: Nantes Université, CNRS, Institut des Matériaux de Nantes Jean Rouxel, IMN, F-44000 Nantes, France.
3: Nantes Université, Ecole Centrale Nantes, CNRS, Institut de Recherche en Génie Civil et Mécanique, GeM, F-44600 Saint-Nazaire, France.
4: Institut Laue-Langevin, 71 Avenue des Martyrs, 38000 Grenoble, France.

Corresponding authors:

david.gloaguen@univ-nantes.fr

Abstract

The aim of this work is to study the mechanical behavior of 6061 aluminum walls produced by Wire Arc Additive Manufacturing at the different scales of the material. The residual stresses of the parts are characterized on the surface and in the bulk thanks to X-ray and neutron diffraction techniques, respectively. Although the residual stress values determined in the close-surface are low (40 MPa for the maximum value), the mechanical state is different in depth with significant maximum residual stress levels (+/- 100 MPa). Tensile tests carried out on samples extracted from a WAAM wall in three orientations reveal that the mechanical properties of the manufactured material are slightly better compared to conventional material in T6 state. *In situ* X-ray diffraction experiments have also been performed under uniaxial tensile testing in order to determine strain pole figures. An elasto-plastic self-consistent model considering the microstructural characteristics and the main physical phenomena governing the material behavior, is proposed. The model agrees

with the experimental data and the simulations reproduce the main features observed at the scale of the diffracting volume.

Keywords

Strain pole figure, X-ray diffraction, Residual stresses, Wire and Arc Additive Manufacturing, Mechanical properties.

Introduction

In some cases, Additive Manufacturing (AM) allows to optimize the mechanical performance of a part while minimizing its environmental impact through reduced energetic and material use. Wire Arc Additive Manufacturing (WAAM) is an innovative concept derived from arc welding processes [1–3] that can be used for AM. It enables to improve the freedom of part design without being limited by a closed chamber. It is also one of the techniques with the highest deposition rates in AM of metallic materials leading to the capability to manufacture large meter-scale components at a lower cost [1,4]. Age hardened aluminum alloys such as aluminum 6061 (AA6061) are widely used in many structural applications due to some of their noteworthy properties such as high specific strength combined with a natural corrosion resistance. However, their well-known poor weldability [5,6] have made them very poor material candidates for AM processes. The recent development of a MIG (Metal Inert Gas) deposition process, based on a low-energy short-circuit transfer mode and called CMT (Cold Metal Transfer), have brought about a major change, making it possible to weld age hardened AA6061 [7–10]. However, those CMT-related studies have been limited to simple welding. In a very recent study [11], we have shown that it is possible to obtain

defect-free parts with the AA6061 using the WAAM process. In this study, wall samples were successfully built using two different deposition strategies. The obtained micro- and macro-structures have been found highly dependent on both process parameters and deposition strategy although both employed deposition strategies produced stacked structures composed of successive alternating layers of columnar and equiaxial grains. In addition, after heat treatment, a higher hardness was obtained for the built parts as compared to conventional forged products. In this previous study, the microstructure of AA6061 parts has then been analyzed in order to understand these hardening phenomena.

However, residual stresses developed during the WAAM building process have an obvious critical influence on the mechanical performance of the part, potentially leading to delamination from the supporting structure, part distortion or crack formation [12,13]. Those residual stresses arise from the high cooling rates, thermal gradients and volumetric changes due to phase transformations occurring over the building process and that are strongly related to the process parameters (heat input, welding speed, wire feed speed and welding trajectories) [14].

Amazingly, although aluminum is one of the most widely used alloys for AM techniques like WAAM [2,15,16], to date, no detailed studies on the mechanical behavior and the residual stress development are available, especially as regard to AA6061 [2,17]. Notwithstanding, the optimization of this technology necessarily requires an in-depth knowledge of the residual stress field being built in the parts as a function of the process parameters in order to ensure reliable performances. Moreover, in order to control the properties of the manufactured parts, it is also necessary to study in detail the influence of this process parameters on the mechanical properties at the different scales of the material.

The present work aims to study the influence of the WAAM manufacturing process and its related parameters on the mechanical properties.

First, the mechanical state of the parts has been characterized in the close-surface and in the bulk thanks to X-ray and neutron diffraction techniques, respectively. The residual stress analysis is actually a requirement to understand the mechanical behavior of the manufactured parts and to possibly optimize the process parameters and/or the post manufacturing heat treatment.

Secondly, tensile tests have subsequently been carried out to obtain the main features concerning the elastoplastic behavior of the material with respect to the process-induced microstructure. Finally, a multiscale modeling of the elastoplastic behavior of the wire-arc additive manufactured 6061 aluminum alloy is proposed. The modeling used in this work is based on a mean field approach (Elasto-Plastic Self-Consistent model, EPSC model) considering the microstructural characteristics and the main physical phenomena governing the material behavior. The purpose was hence to develop a tool to better understand the relationship between the mechanical properties and the microstructures produced by WAAM (grain sizes, crystallographic and morphological textures ...). This modeling was coupled with *in situ* X-ray diffraction tensile experiments.

I. Experiment

I.1. Material and deposition process

Since the deposition process has been extensively presented in a previous work [11], only a brief description will be done here. For this study, AA1050 aluminum alloy was used as substrate (plates with a size of $2 \times 30 \times 250$ mm^3) and a 1.2 mm diameter of AA6061 alloy wire was chosen as the filling material. The measured chemical composition of the welding wire is listed in Table 1.

AA6061 thin-wall samples with dimensions 150 (x) × 5 (y) × 55 (z) mm^3 have been deposited by the MIG-CMT process developed by Fronius®. Each layer of these walls was deposited in a single pass. Fore sake of clarity, three directions are set as follow: x, along the welding direction; y, perpendicular to the travel direction of the welding torch and z, along the building direction. A Cartesian robot with step-by-step motors equipped with a Fronius® TransPuls Synergic 3200 CMT welding device composed the experimental set-up. The welding torch working distance was set constant at 15 mm. A water-cooling system regulated the bottom of the clamped AA1050 baseplate at 20 °C. Wire feed rate was set at 4.3 $m.min^{-1}$ and travel speed at 320 $mm.min^{-1}$. A mixture of argon and helium in a ratio of 80/20 has been used as shielding gas. Two deposition strategies (in terms of torch trajectories sequence) were studied: unidirectional deposition (deposition without change in the welding direction) and bidirectional deposition (with two alternating opposite deposition directions).

Elements	Mg	Si	Cr	Fe	Ti	Zn	Mn	Cu	Al
AA6061 wt%	0.9	1.0	0.1	0.3	-	0.2	0.1	0.2	Bal.

Table 1: chemical composition of the AA6061 welding wire measured using EDS.

The grain structures were analyzed by EBSD. Results are depicted in Figure 1 in the form of inverse pole figure maps along the transverse direction y. The microstructure was examined in the middle of the wall, in order to avoid the effects of arc initiation and extinction. Observations were also made at different heights in the wall, as the microstructure of the first and last layers differs from the remainder of the wall. The results presented here are based on mid-height observations.

Both unidirectional and bidirectional strategies induce the same structure of layers. This structure is composed of a stack of alternating equiaxed and columnar grains zones. Each deposited layer is made of columnar grains that epitaxially grow from the previously solidified grains present on the surface of the previous layer. A thinner zone of equiaxed grains is located at the top of each layer. Each new built layer partially melts the previous one. The growth direction of the columnar grains is related to the deposition direction (through the heat gradient that set during deposition). Thus, the bidirectional strategy, which alternates two opposite deposition directions, produces columnar grains growing along two alternating solidification directions, symmetrically distributed with respect to the transverse plane (y-z), while the unidirectional strategy maintains the same solidification direction layer after layer. The unidirectional strategy gives a single growth direction, resulting in a sharp <100> texture component in the x + 65° direction, as illustrated in the pole figures in Figure 1. The alternating strategy gives a more balanced texture with two reinforcements matching the two preferential solidification directions.

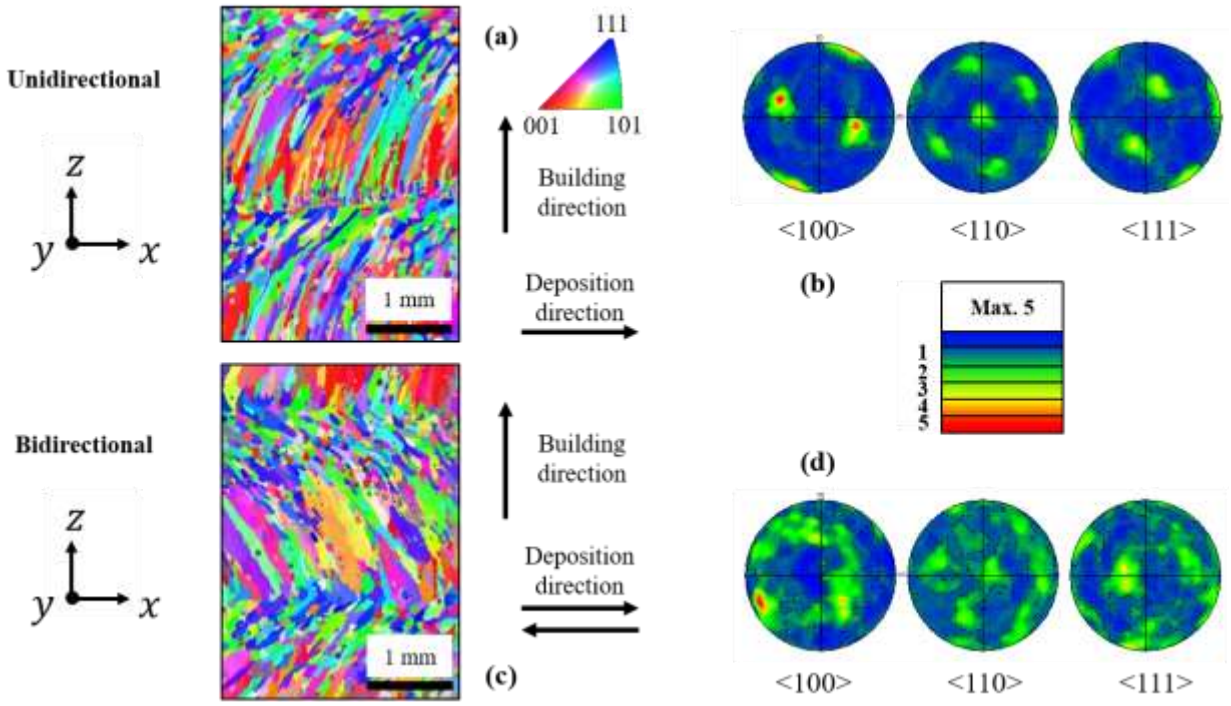

Figure 1: EBSD maps for WAAM samples built; (a) with the unidirectional strategy and (c) with the bidirectional strategy. (b) and (d) show their respective pole figures.

For the residual stress determination, different walls have been built for this study. The analysis was performed for the two deposition strategies and for two metallurgical states as follows:

- As-Deposited (denoted AD): material has simply been kept at -80 °C directly after printing in order to prevent it from natural aging,
- T6 heat treatment (denoted T6): solid solutionizing at 530 °C during 1 h + quenching (water cooling) + artificial aging at 175 °C during 8 h.

Concerning the *in situ* X-ray diffraction tensile experiments, the testing was performed with the material in T6 condition built with the bidirectional strategy.

I.2. Subsurface residual stress analysis by X-ray diffraction

The average lattice strain within the diffracting volume V_d can be calculated from the shift of measured Bragg's angle, $\theta(\varphi, \psi, hkl)$, along the measurement direction defined by the angles (φ, ψ) for a $\{hkl\}$ reflection, as compared to its value in the stress-free material, as detailed in equation (1) [18]:

$$\langle \varepsilon(\varphi, \psi, hkl) \rangle_{Vd} = ln\left(\frac{sin\theta_0(hkl)}{sin\theta(\varphi, \psi, hkl)}\right) \quad (1)$$

$\langle\ \rangle_{Vd}$ corresponds to an averaging operation over the diffracting volume V_d. θ_0 is the Bragg's angle of the stress-free material. In the case of a homogeneous and macroscopically elastically isotropic single-phase polycrystal, neglecting plastic deformation incompatibilities, the traditional equation for X-ray stress analysis is given with the $sin^2\psi$ method as:

$$\langle \varepsilon(hkl, \varphi, \psi) \rangle_{V_d} = \frac{1}{2} S_2(hkl)(\sigma_{11} cos^2\varphi + \sigma_{12} sin2\varphi + \sigma_{22} sin^2\varphi)\ sin^2\psi +$$

$$\frac{1}{2} S_2(hkl)(\sigma_{13} cos\varphi + \sigma_{23} sin\varphi)\ sin2\psi + + S_1(hkl)(\sigma_{11} + \sigma_{22}) \quad (2)$$

Where ½ S_2(hkl) and S_1(hkl) are the so-called X-ray Elastic Constants (XEC), σ_{ij} the components of the Cauchy's stress tensor in the sample orthonormal coordinates system (1, 2, 3). Regarding the XRD set-up used to perform the experiments, indexes 1, 2 and 3 respectively refer to the z, x and y directions of the part, defined ahead. It is usually assumed that, because XRD is a near-surface analysis, the diagonal component related to the normal to the analyzed surface direction - i.e. σ_{33} component - is equal to zero due to the low penetration depth (19.9 µm for $sin^2\psi = 0.3$ with Co radiation). Note that with this assumption, information about the real stress-free lattice parameter $\theta_0(hkl)$ is then no more necessary. In the present XRD analysis set-up, σ_{33} sample

coordinates matches σ_{yy} in the part i.e. stress related to the perpendicular to the travel direction of the welding torch.

Residual stress analyses were carried out with a four-circle Seifert XRD 3003 PTS diffractometer with a cobalt radiation. The X-ray beam output collimator was 1 mm in diameter. The diffraction peaks were recorded with a position sensitive detector. The determination of residual stresses was conducted using the $sin^2\psi$ method with the {331} diffraction peak at $2\theta \approx 149°$. Diffractograms were recorded for sixteen different tilt angles ψ varying between -48° and 45° and for azimuth angles φ of 0°, 45° and 90°. The direction $\varphi = 0°$ corresponds to the welding direction. Peak positions were calculated using a pseudo-Voigt fitting function for the measured peak considering the dual $K_{\alpha1}$–$K_{\alpha2}$ contribution. Since the studied material displays large grains, oscillations of the ψ angle ($\Delta\psi$: +/-5°) have been performed during the measurements so as to analyze a larger volume of material, optimizing the residual stress measurement conditions. The subsequent error induced has been demonstrated to be no more than 2 % on the stress values for the chosen oscillation magnitude [18,19]. The stress field investigation has been performed along a line following the building direction z in the middle of the sample in order to ensure analysis in the stationary regime. Ten different positions, distributed over the height of the wall, have been probed by XRD.

I.3. Bulk residual stress analysis by neutron diffraction

In order to determine the stresses in the bulk sample, additional Neutron Diffraction (ND) experiments have been carried out on the SALSA beamline [20] at the Institut Laue Langevin (ILL) in Grenoble (France). The gauge volume in the sample was set to 2×2×2 mm^3 with a wavelength of 1.62 Å as a compromise between grain size, mapping resolution and reasonable measurement

duration. The stress determination was performed by recording the {311} diffraction peak ($2\theta \approx 88.5°$).

The stress field investigation has been performed along a column set in the middle of the sample as for XRD investigations. Single peak fitting was performed using the LAMP software [21] enabling to obtain the peaks positions by fitting the experimental data with a pseudo-Voigt function and a polynomial background.

For each measurement point, lattice strains were determined along the three orthogonal directions x, y and z of the part to provide an evaluation of the three normal strain components $\langle\varepsilon(0{,}90, hkl)\rangle_{V_d} = \varepsilon_{xx}$, $\langle\varepsilon(90{,}90, hkl)\rangle_{V_d} = \varepsilon_{yy}$ and $\langle\varepsilon(0{,}0, hkl)\rangle_{V_d} = \varepsilon_{zz}$.

With eq. (2), the normal stress components σ_{xx}, σ_{yy}, σ_{zz} are calculated [22].

Lattice strains within the diffracting volume are calculated from the Bragg's angle shift (Eq. (1)). In order to ensure reliable θ_0 measurements, especially regarding the possible evolution of the metallurgical state, the chemical composition and/or the microstructure during the building process, a specific procedure has been used, which is extensively detailed in [23]. The Bragg's angle of the stress-free material for each measurement point has been acquired thanks to measurements carried out over a series of mini-cubes of 4×4×4 mm^3 cut thanks to electro-discharge from twin specimens (manufactured with the same process parameters) and matching the exact positions of the ND stress analyses of the walls. Cutting small coupon intends to relieve any macroscopic stress. In order to ensure that potential residual intergranular strains present in these mini-cubes do not interfere with the stress-free parameter determination, measurements have been achieved along numerous directions and then averaged.

I.4. XEC determination method by XRD

The residual stress analysis through XRD or ND requires the accurate knowledge of the XEC, ½ S_2(hkl) and S_1(hkl). The XEC values for aluminum alloys can greatly vary according to the considered type of alloy, the quantity of alloying elements and the precipitation state [24,25]. No experimental value is actually available in the literature for the one studied in this work. It is therefore relevant to experimentally determine the XEC in order to consider the precipitation state and the microstructural parameters inherent to the studied parts.

These XEC can be determined when a sample is elastically loaded *in situ* in a diffractometer and the corresponding lattice strains are measured for different sample orientations and applied loads [18,26]. In this method, a quasi-isotropic single-phase material having no preferential crystallographic orientation (i.e. elastically anisotropic grains in a randomly distributed crystallographic orientation sample) is then assumed.

A known macroscopic stress σ^A is applied to the studied sample and the lattice strain $\langle\varepsilon(\varphi,\psi,hkl)\rangle_{V_d}$ is measured as a function of this mechanical stress. If a uniaxial tensile test is performed σ_{11}^A, the relation between the lattice strain and the average stress is:

Where 1 refers to longitudinal direction of the dogbone-shaped tensile specimen.

$$\langle\varepsilon(\varphi,\psi,hkl)\rangle_{V_d} = \frac{1}{2}S_2(hkl)[\sigma_{11}^A cos^2\varphi]sin^2\psi + +S_1(hkl)[\sigma_{11}^A] \quad (3)$$

At φ = 0°, we finally obtain:

$$\langle\varepsilon(\varphi,\psi,hkl)\rangle_{V_d} = \frac{1}{2}S_2(hkl)\sigma_{11}^A sin^2\psi + +S_1(hkl)\sigma_{11}^A \quad (4)$$

225 $\langle\varepsilon\big((0,\psi,hkl)\big)\rangle_{V_d}$ is measured for different values of the applied stress (σ_{11}^A) and different values
226 of declination angle (ψ). The equation (4) can be used to fit XECs when $\sigma_{11}^A$is known. The
227 measured $\langle\varepsilon(0,\psi,hkl)\rangle_{V_d}$ values can be plotted according to $sin^2\psi$ for different applied loads. If
228 the texture influence is negligible, these curves can be fitted by linear functions. The slopes (resp.
229 the intercepts) of these fits can be plotted versus the applied stress σ_{11}^A, and then fitted with a linear
230 function where the resulting slope is the $\frac{1}{2}S_2(hkl)$ XEC (resp. $S_1(hkl)$).

231 Flat dog-bone tensile specimens with a strain gauge section of 13.65 × 8 × 1 mm^3 were cut out by
232 electro-discharge machining from the thin-walls samples considering three different directions
233 with regard to the Welding Direction (WD): parallel (denoted WD), perpendicular (denoted BD
234 for Building Direction) and inclined at -65° from the deposition direction (denoted GD for Grain
235 Direction). For the last tensile sample, the tensile direction is parallel with the long axis of the
236 grains (see Fig. 1). *In situ* tensile tests were performed at room temperature within a four-circle
237 Seifert XRD 3003 PTS diffractometer with a Co-K_α radiation and using a Deben tensile device
238 adaptable to the Eulerian cradle of the goniometer. *In situ* lattice strain measurements, performed
239 on {331} diffraction peak, were conducted in load-control mode with a load cell of 5000 N capacity
240 and 0.1 N resolution. The $\langle\varepsilon(\varphi,\psi,hkl)\rangle_{V_d}$ lattice strains were calculated with equation (1). In this
241 case, θ_0 is the initial Bragg's angle of the sample at 0 MPa - i.e. when no load is applied. This
242 reference angle has been measured in the undeformed samples for each probed direction (0,ψ):
243 $\theta_0(0,\psi,331)$. The measured lattice strains are therefore elastic strains induced by the mechanical
244 loading and do not consider the potential contributions from residual strains due to the process. It
245 should be however noticed that although residual stresses (see section III.2) exist in the built thin-
246 wall, tensile sample machining actually removes the constraint provided by the remainder of the
247 wall so that the macroscopic stresses will be mostly relaxed in the studied samples. The

experimental procedure consists in loading the sample at various load magnitudes, in the elastic regime: 0, 20, 40, 60, 80, 100, 120, 140, 160, 180 MPa and for several specimen orientations: $\varphi = 0°$ and $\psi = \{0°; 6°; 12°; 18°; 24°; 30°; 36°; 42°,48°\}$.

I.5. *In situ* measured strain pole figures

In situ XRD analysis have been achieved under uniaxial tensile testing in order to determine strain pole figures in elasto-plasticity for the three tensile specimens (WD, BD and GD) and to quantify the influence of microstructural parameters (texture and grain shape) on the global mechanical behavior. The same experimental setup presented in the previous section has been used. During the *in situ* diffraction experiments, data were collected at 5 given macroscopic strain levels (0, 0.2, 0.5, 0.8 and 3 %) for several specimen orientations. The samples were speckled, and images were recorded during the test. Digital image correlation was then processed to obtain the macroscopic total strain fields.

Incomplete strain pole figures were measured with tilt and azimuth angles ranging from 0° to 50° and from 0° to 90°, respectively, at each chosen total strain state. diffractograms were recorded along different (φ,ψ) directions with a step of 5° for both ψ and φ angles. The φ upper value was limited to 50° owing to the shadowing of the tensile device. In order to determine the corresponding incomplete strain pole figure, a total of 209 diffractograms were recorded for each deformation step. For these investigations, at $\psi = 90°$ and $\varphi = 90°$, the scattering vector $\boldsymbol{Q}$ was aligned with the Longitudinal Direction (denoted LD – i.e. the loading direction). $\boldsymbol{Q}$ was parallel to the Transverse Direction (denoted TD) at $\psi = 90°$ and $\varphi = 0°$. The lattice strains $\langle \varepsilon(\varphi, \psi, hkl) \rangle_{V_d}$ were calculated with equation (1). The reference Bragg's angle has been measured in the undeformed samples for the $\{331\}$ diffracting peak and for each (φ, ψ) direction: $\theta_0(\varphi, \psi, 331)$.

II. Model

A mean field approach, the self-consistent model, has been used to describe the mechanical behavior and to interpret the collected diffraction data. The objective is to replace the real heterogeneous material with a fictitious homogeneous material which has the same behavior at the macroscopic scale by using a homogenization procedure. In the present work, the model developed in [27] is used and will not be described in details here. For FCC metals, the plastic deformation was simulated assuming $\{110\}\langle 111\rangle$ slip systems. Each grain is supposed to be an ellipsoidal elastoplastic inclusion, embedded in an elastoplastic Equivalent Homogeneous Medium (EHM) representing the average properties of all the grains in the polycrystal. The EPSC model has the capability to account for the crystallographic and morphological (grain-shape) textures of the material [28]. Each grain is described by an elastic constant tensor, crystallographic slip directions and planes in order to predict the strain/stress state of the grain under a mechanical load. A hardening matrix, H^{gh}, is introduced to describe the CRSS (Critical Resolved Shear Stress) changes with strain for each deformation mode g, as a function of the plastic slip on the other deformation systems h for each grain:

$$\dot{\tau}_c^g = \sum_h H^{gh}\dot{\gamma}^h \quad (4)$$

$\dot{\gamma}^h$ is the plastic slip rate on the h-th active system. H^{gh} are the hardening coefficients that characterize self- (with $h = g$) and latent- (with $h \neq g$) hardening between deformation systems g and h.

The latent hardening coefficients are assumed to be described as follow [29]:

$$H^{gh} = qH^{gg} \ (g \neq h) \quad (5)$$

The q factor defines the degree of latent hardening. This factor is chosen in order to provide the best accordance between the experimental and simulated and stress-strain curves in plasticity.

Due to the lack of data for AA6061 alloy, the elastic constants of aluminum single-crystal used in the simulation are assumed to be those of pure aluminum [18]: c_{11} = 108.2, c_{12} = 60 and c_{44} = 28.5 MPa.

The CRSS value was chosen in order to reproduce the elastoplastic transition observed on the macroscopic stress – strain curve for the sample WD. The same value was used to simulate the behavior along the two other loading directions.

The EPSC model has the capability to account for the grain-shape and its evolution. Based on EBSD results, the simulation considers that the shape of the inclusion (grain) is ellipsoidal with half axes defined by a, b and c so that $a = 2.5 \neq b = c = 1$. The initial texture is represented by a discrete distribution of 2000 ellipsoidal grains with Euler angle orientations weighted to reproduce the crystallographic texture shown in Figure 1. The grain orientation and crystallographic texture used to simulate the behavior of the WD, BD and GD samples are detailed in Figure 2. In the case of the WD sample, the inclusion long-axis x_e of the ellipsoid coordinates system (x_e, y_e, z_e) is tilted by an angle $\alpha = 65°$ from the y-axis of the part coordinates system (x, y, z). In the case of the BD sample, $\alpha = 25°$. For the GD sample, the ellipsoid coordinates system coincides with the one of the part.

Sample	Half-axis length and tilt angles	Grain morphologies and orientations	Crystallographic textures {100} {110} {111}	Schematic representation of the simulation
BD	$a_1 = 2.5$ $a_2 = 1$ $a_3 = 1$ $\alpha = 25°$	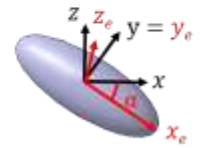		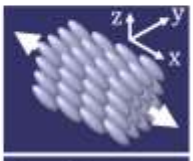
WD	$a_1 = 2.5$ $a_2 = 1$ $a_3 = 1$ $\alpha = 65°$	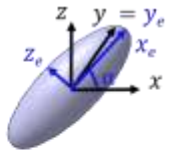	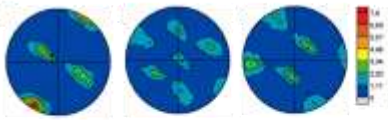	
GD	$a_1 = 2.5$ $a_2 = 1$ $a_3 = 1$ $\alpha = 0°$	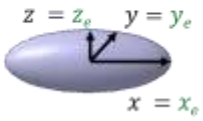	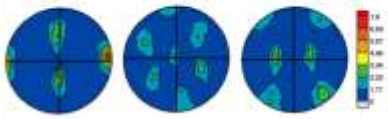	

Figure 2: grain orientation and crystallographic texture used to simulate the behavior of the WD, GD and BD samples.

The set of material parameter values giving the best agreement between the simulated and the measurements are presented in Table 2.

H^{gg} (MPa)	τ_c^g (MPa)	q
30	115	1.1

Tables 2: material parameters used in the simulations.

III. Results and discussion

III.1. XEC

Based on the procedure described in section I.4 and using Eq. (4), XECs can be estimated by plotting the slope (Fig. 3.a) and intercept (Fig. 3.b) of the linear regression versus the applied macroscopic stress. The resulting data show a clear linear dependence with the applied macroscopic stress. According to the explanations given in section I.4, the slope of these linear functions corresponds respectively to $\frac{1}{2}S_2(hkl)$ and $S_1(hkl)$. The correlation coefficients, R^2, are very close to 1 and, *a posteriori*, demonstrate the validity of assuming an isotropic macroscopic mechanical behavior for the material.

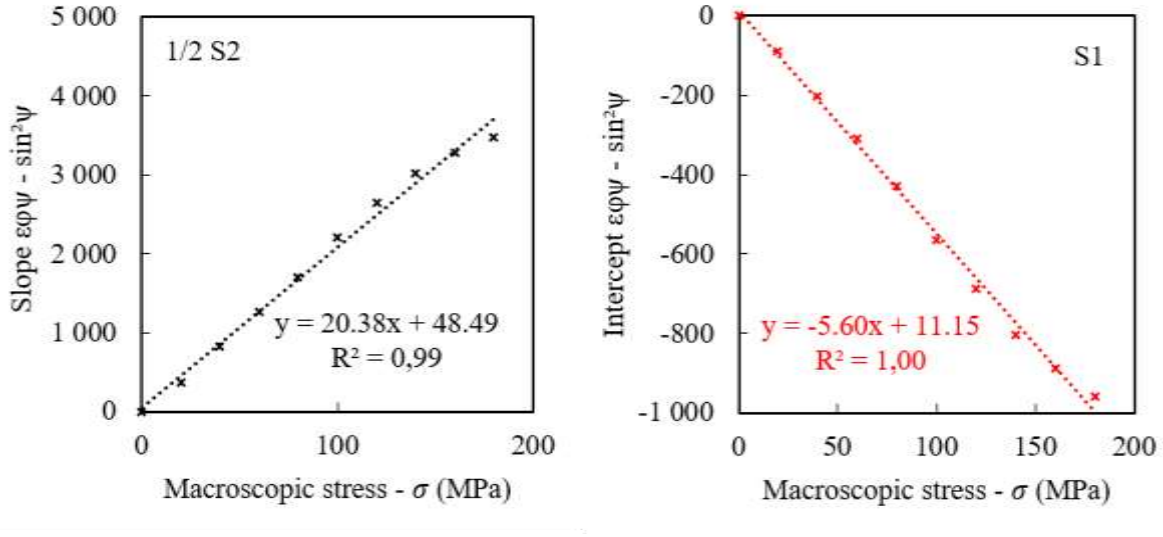

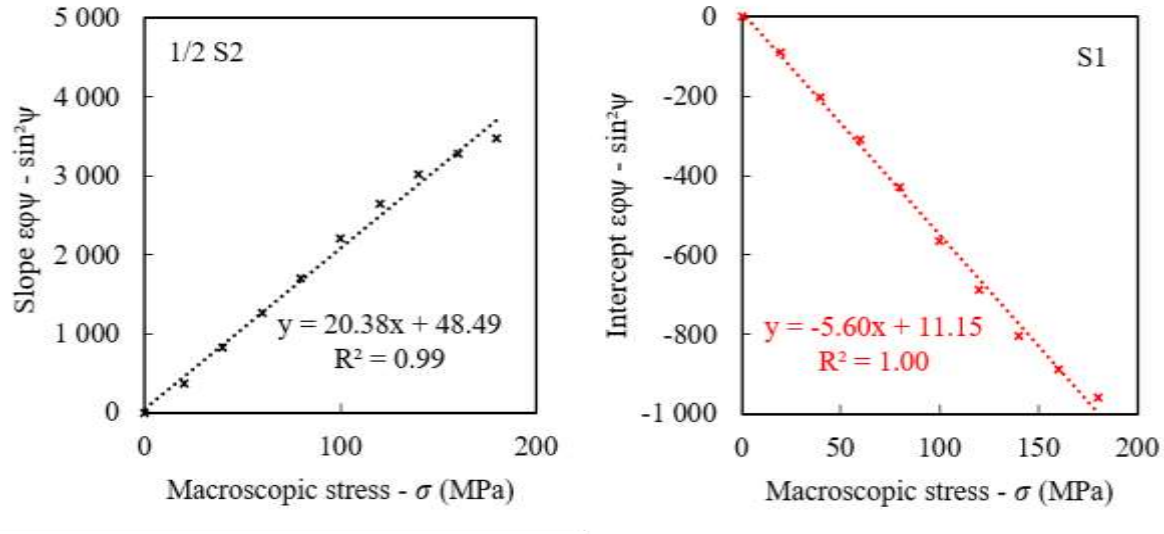

(a) (b)

Figure 3: line fitting data from the procedure described in section I.4: a) slope and b) intercept versus the applied stress.

These values were obtained for the 3 specimens collected in the three directions WD, BD and GD. The results are summarized in Table 3. They do not show significant differences.

The XECs, ½ S2{hkl} and S1{hkl}, can also be calculated by modeling the behavior of the polycrystalline aggregate [27,30]. Therefore, these constants were also calculated using an elastic self-consistent model [27] with the elastic constants of the pure aluminum single-crystal (c_{11} = 108.2 GPa, c_{12}= 60 GPa, and c_{44} = 28.5 GPa [18], commonly used in the literature). These values can also be compared with those obtained in the literature for other aluminum alloys (see Table 3).

Tensile sample	$\frac{1}{2}S_2(hkl)$ ($\times 10^{-6}$ MPa^{-1})	$S_1(hkl)$ ($\times 10^{-6}$ MPa^{-1})
BD	20.4	-5.6
GD	22.4	-6.2
WD	21.3	-5.6
Mean value	21.3 +/ -1.0	-5.8 +/ -0.4
Elastic self-consistent simulation	19.2	-4.9
Pure Al [18]	18.9	-4.9
Al-2014-T6 [31]	16.8	-
Al-2024-T351 [31]	18.6	-
Al-7075 T6 [31]	17.5	-

Table 3: comparison of the experimental XECs with values from the literature and the values obtained with the elastic self-consistent model.

It can be noted that the experimental values are relatively different (about 10 %) from those obtained by modeling or those gathered from the literature for pure aluminum. The alloying elements present in the material as well as the distortion of the matrix around the precipitates can modify the XEC values [24,25]. This difference between pure aluminum and its alloys seems to be confirmed by the experimental values available for other types of aluminum alloys (Table 3). In the light of the weak differences observed in the three directions as well as the significant difference between the experimental values and the available data (calculation and literature) for pure aluminum, we thus made the choice to use the average values obtained experimentally for the stress analysis by XRD: $\frac{1}{2}S_2(331) = 21.3\ 10^{-6}MPa^{-1}$ and $S_1(331) = -5.8\ 10^{-6}MPa^{-1}$. Note that the same XEC values have been used for the data analysis obtained by ND due to the quasi macroscopic elastic isotropy of the studied material.

III.2. Residual stresses

The stress profiles determined on the surface for each measured point distributed over the height z of the walls are shown in Figure 4. The position z = 0 mm corresponds to the top surface of the substrate. As a reminder, the σ_{33} stress in the direction normal to the probed surface is assumed to be null in the case of XRD analysis. This stress component actually matches σ_{yy} stress in the part coordinates system - i.e. along the transverse direction of the wall.

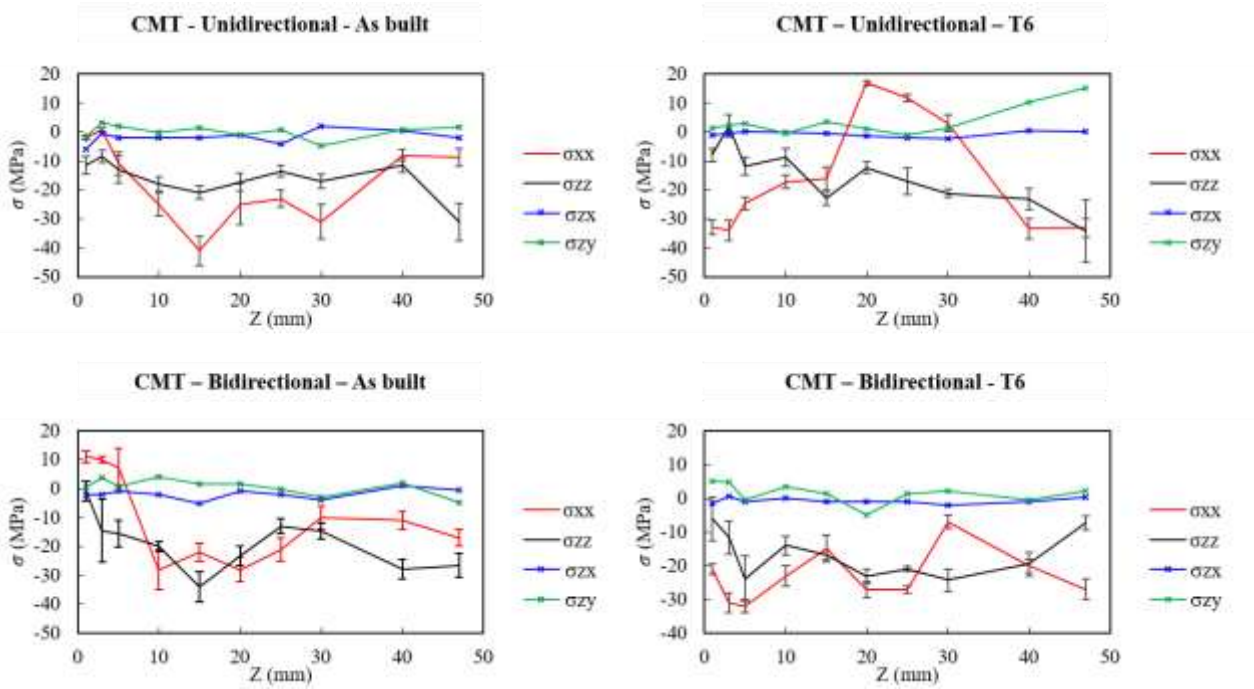

Figure 4: residual stress analysis by XRD along the welding (WD, x-direction) and building (BD, z-direction) directions versus the distance from top surface of baseplate.

Whatever the printed sample analyzed, very low and similar levels of residual stresses are found. It seems that either the fabrication process completely relaxes the stresses or edge effects are responsible for the removal of residual stresses from the surface. The analyses have been conducted on surfaces in direct contact with the surrounding atmosphere. The stress level is globally

equivalent throughout the height of the different walls. Although residual stress values are low in the probed close-surface volume (with a maximum of 23 MPa for the average values and 40 MPa for the maximum value), the mechanical state might be different for deeper probed volumes.

ND experiments are thus relevant since it provides additional information leading to a better understanding of the mechanical state of the parts produced by WAAM. Significant maximum residual stress levels, more than +/- 100 MPa, are observed in the three measurement directions as observed in Figure 5. The maxima observed are as follow:

σ_{xx} = +/- 119 MPa, σ_{yy} = +/- 105 MPa, σ_{zz} = +/- 110 MPa.

Slightly higher residual stress values were observed along the welding direction (x). These results are in agreement with the literature for other alloys [13,14,32]. However, the measured values in the two other directions are quite close, in contrast to the values observed in these previous works. Unidirectional and bidirectional strategies give similar stress levels and the same type of variations along the three main directions x, y and z. The same trend is observed for the T6 heat treatment with a modification of the stress profile.

In this study, the effect of arc mode type in cold metal transfer (CMT) process on the residual stress evolution has been also studied. More specifically, the cold metal transfer pulse (CMT-P) process [33] which is a combination of traditional CMT welding process and pulse welding process, was employed and its influence on the residual stress was analyzed. AA6061 thin-wall samples with the same dimensions (i.e. 150 (x) × 5 (y) × 55 (z) mm^3) have been deposited using the MIG-CMT-P process with the bidirectional strategy. Figure 5 compares the residual stress distribution obtained with CMT-P and CMT processes.

In the case of CMT-P process, we find the trends observed by different authors [13,14,32] for other alloys. When the part has just been deposited by WAAM and is still clamped to the substrate, the stresses are generally more tensile in the wall and compressive in the substrate. During unclamping, more freedom is brought to the system baseplate + wall, with a reorganization of the mechanical fields. The part tends to contract at the top and expand near the baseplate. This is why distortions are observed. These distortions are accompanied by a redistribution of internal stresses. The stresses decrease with the height of the wall and can even reach compression at the top of the wall. In the baseplate, the stress evolves in the opposite way until it reaches tension in the lower part. In the transition zone between the baseplate and the first deposited layers, the tensile stresses reach a maximum.

As shown in Figure 5, in the case of CMT process, the observed trends are different. The residual stress values are negative (compression at Z = - 4 mm) within the baseplate. The stress profile evolves rapidly from the first layers towards tensile stress values. A maximum is reached in the first layers of the wall (close to the baseplate). A second tensile maximum is observed in the last layers (Z = 40 mm) and the stresses remain relatively low between these two points. In the case of CMT process, the sample shows a stress profile similar to a clamped sample as described in the literature (compressive stress in the substrate and tensile stress in the wall [14]). It is possible that the clamping conditions or the deposition setup have allowed the substrate more freedom to deform during deposition, leading to a different stress distribution.

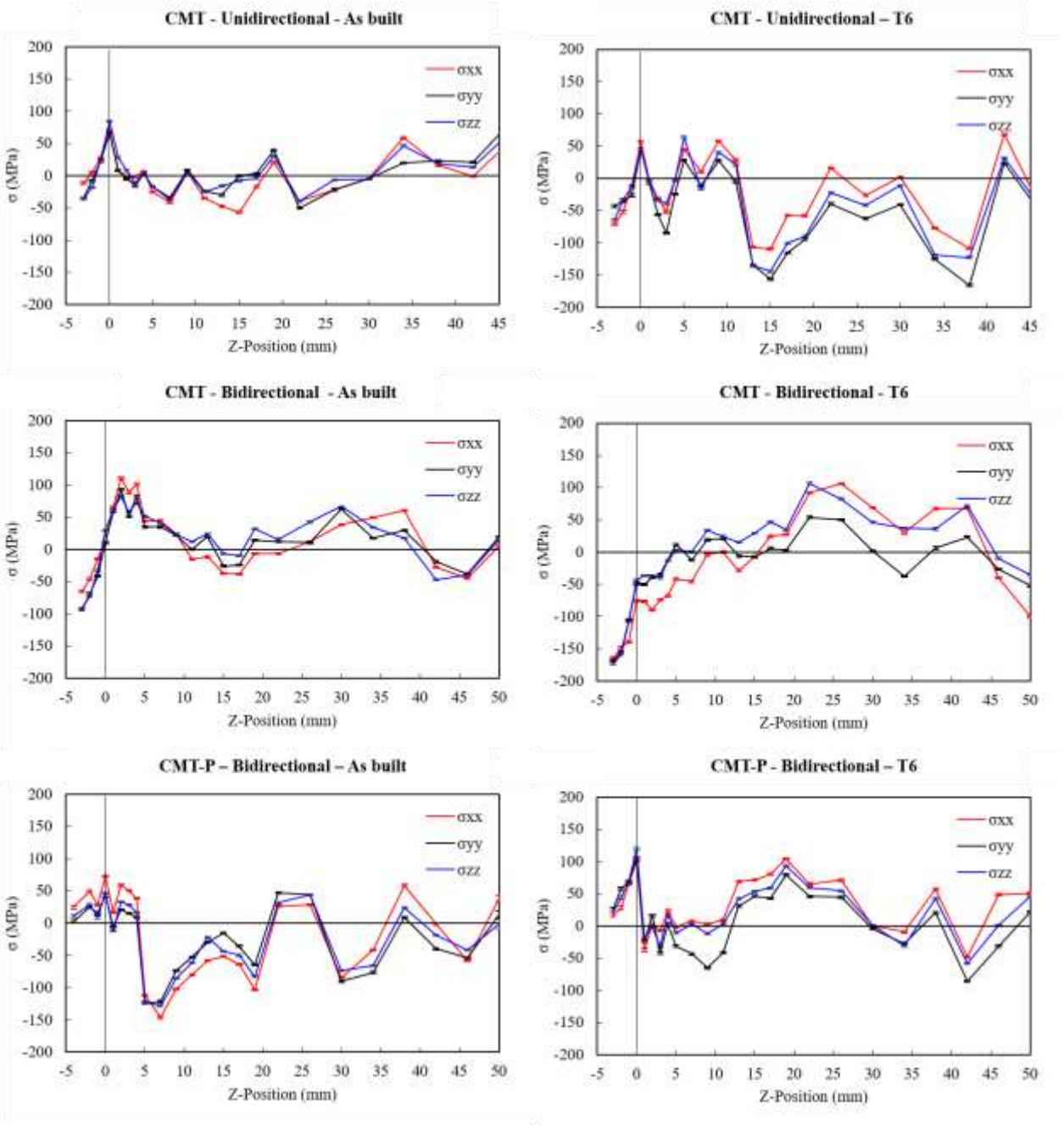

Figure 5: residual stress distribution obtained by ND with CMT and CMT-P processes for unidirectional and bidirectional strategies.

To explain the difference between residual stress values in the probed close-surface volume and the mechanical state for deeper probed volumes, it should be recall that the residual stresses

421 determined by XRD only concern the near-surface zone of the material and vary between -40MPa
422 and 10MPa with a predominantly compressive state. These stresses are low, whereas the stresses
423 determined by ND in the core sample show larger variations (between -150MPa and 100MPa) and
424 mechanical states that are locally compressive which turn into tension in other regions. If we
425 consider the walls (without considering the substrate) in the AD material, the range is smaller (-50
426 MPa, 100 MPa) but remains larger than the values obtained at the surface. Internal stresses develop
427 in built components due to the high cooling rates, the thermal gradients and the volumetric changes
428 arising during phase transformations occurring during the process. Thermal gradients tend to
429 induce tensile stresses in the last deposited layer. The residual stresses decrease and could thus
430 even reach negative values in the underlying layers [34]. The highest stress values are generally
431 observed near the substrate. This is consistent with the results observed for the AD material with
432 the unidirectional strategy and the CMT process. The effect of microstructure is more difficult to
433 understand, and the material used here is particularly sensitive to this effect since it is a
434 precipitation-hardened aluminum alloy. T6 treatment, which significantly modifies the
435 microstructure, changes the stress profile, as shown by the results obtained in Figure 5 (CMT-P
436 Bidirectional, CMT Bidirectional and CMT Unidirectional) before and after treatment. As surface
437 cooling conditions are specific, it is logical to determine residual surface stresses (XRD) different
438 from the stresses obtained in the bulk (ND).

439

440 **III.3. Mechanical properties**

441 The results obtained at the macroscopic scale with the *in situ* tensile tests allowed to achieve the
442 tensile curves. It should be noted that the maximum imposed strain is 7 % due to a systematic
443 unexpected stop of the tensile machine after a very large number of measurements during the XRD

444 tests. The results of the tensile tests for the 3 three specimen orientations (WD, BD, GD) have been
445 compared to a reference sample extracted from a rolled plate in T6 condition and are presented in
446 Figure 6.

447

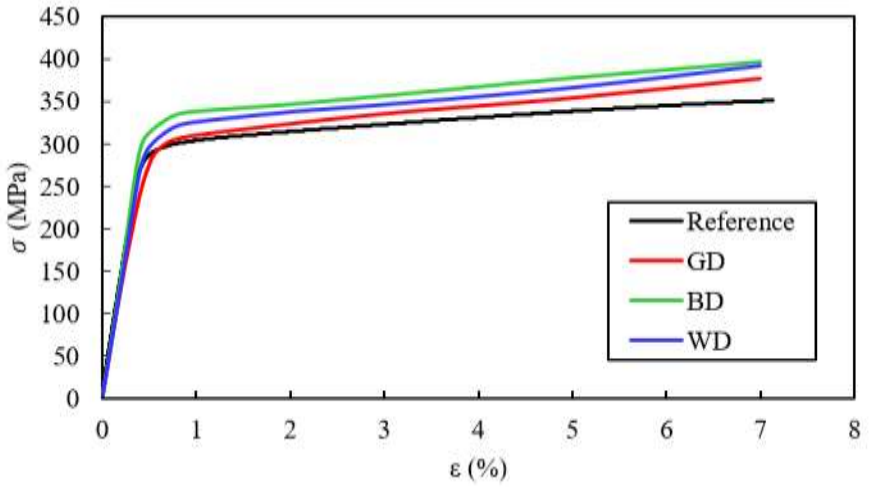

448

449 Figure 6: stress-strain curves for WD, BD and GD tensile specimens compared to the reference
450 sample extracted from a rolled plate in T6 condition.

451

452 The tensile properties of additively manufactured specimens are similar or slightly better than those
453 obtained for the reference sample obtained from a rolled 6061-T6 plate. The related mechanical
454 parameters are summarized in Table 4. The maximum strength R_{ms} recorded at 7 % macroscopic
455 strain is systematically higher than the one observed for the reference specimen. However, no
456 significant difference between the different directions is observed: the presence of equiaxed grains
457 has probably enabled to limit the effect of the columnar grains. It should be noted that the properties
458 of the GD specimen (with the loading direction parallel to the grain growth direction) only show
459 slightly lower properties than the others (especially as regard to the yield strength, R_e). A similar
460 study (results not shown here for the sake of clarity) has been performed with the second deposition

strategy. It has revealed that the two strategies display equivalent mechanical properties, certainly due to the presence of these equiaxed grains. The crystallographic texture for the bidirectional strategy, which is more homogeneous at the part scale due to the two growth directions (Fig. 1), does not seem to have a significant effect on the mechanical properties.

Specimen	R_e (MPa)	R_{ms} (MPa) (at 7 % strain)
Reference	257	351
WD	248	393
BD	261	397
GD	232	378

Table 4: mechanical properties for WD, GD and BD samples.

To complete this study, tensile tests, at room temperature, were carried out on flat specimens, whose geometry and dimensions were chosen according to ISO 6892-1 (gauge length of 33.54 mm, gauge width of 10 mm and nominal thickness of 2.5 mm). To achieve these tests, the specimens were extracted from a block sample (length: 250 mm, height: 80 mm width: 100 mm) manufactured with the CMT-P process. Two specimens for each extraction direction (x-direction or longitudinal direction, y-direction or transverse direction and z-direction or normal direction) were tested (Figure 7).

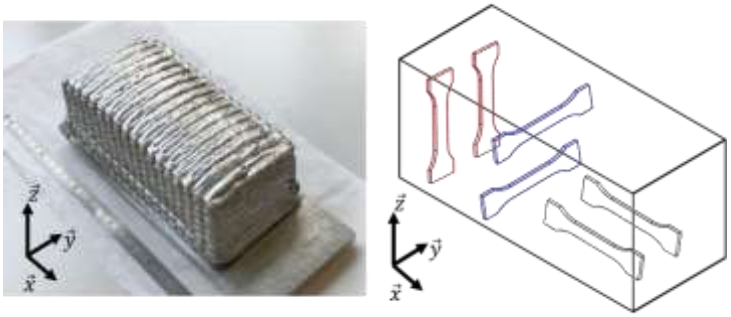

Figure 7: locations for extraction of samples for mechanical tests.

In Figure 8, we can see that one of the specimens collected in the longitudinal direction has a very low elongation compared to the other specimens. A significant quantity of porosity was observed on the failure surface after the mechanical test. However, we do not know the cause of this increased porosity (proximity to the substrate, unmonitored change in electrical parameters...).

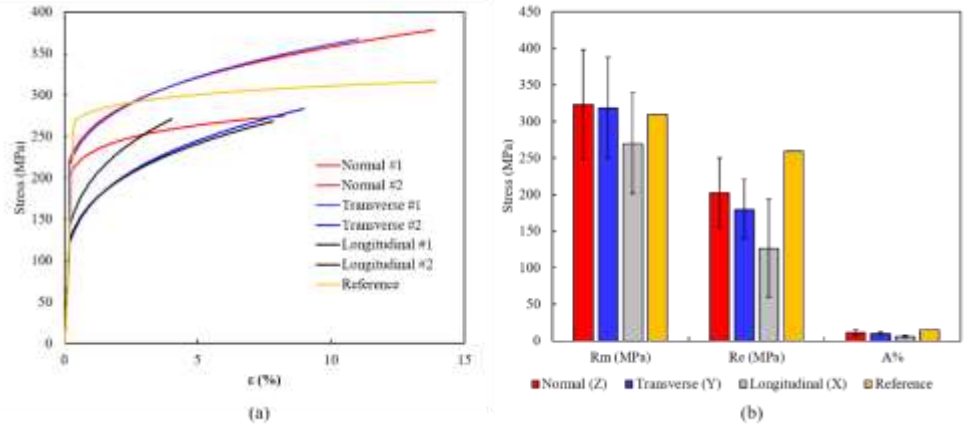

Figure 8: (a) stress–strain curves for tensile tests; (b): comparison of yield strength (Re), ultimate strength (Rm) and elongation data of WAAM samples (reference sample extracted from a rolled plate in T6 condition is also included for comparison).

The measured tensile properties are different due to a number of porosity higher than that of the thin wall samples whatever the testing direction (≈ +/-150 MPa for Rm and ≈ +/-100 MPa for Re). Nevertheless, the tensile properties of the specimens in the normal (Z) and transverse (Y) directions in the block sample are close to those measured in the walls (see Figure 8.b) and in the sample obtained from a rolled 6061-T6 plate. These results confirm the possibility to obtain large-scale aluminum parts with good mechanical properties. Additional investigations on the process parameters should be made to obtain block sample with lower porosities like AA6061 thin-wall samples.

At the macroscopic scale, simulations are in good agreement with the experimental mechanical behavior (Figure 9). They give results close to the experimental values with a maximum stress deviation lower than 2 %. The elastic regime is, moreover, quite well reproduced. The choice of the single set of elastic constants from pure aluminum can therefore be validated at this scale of observation. At the macroscopic scale, the three experimental tensile curves display differences between them. At the onset of plasticity, the curve obtained with the WD specimen is about 5 % above the curve from the GD sample. Similarly, the curve from BD specimen is about 13 % higher than the curve from GD sample. The model closely reproduces this difference: the simulated WD curve is also about 5% above the predicted GD curve and the simulated BD curve is about 12 %. However, simulations slightly underestimate the mechanical behavior during the elastoplastic transition.

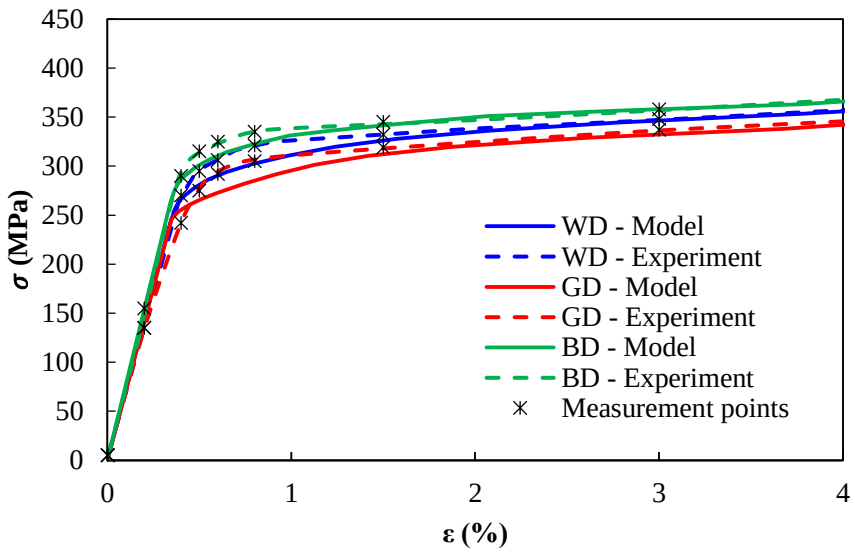

Figure 9: measured (dashed lines) and calculated (solid lines) macroscopic stress vs. macroscopic strain for the three specimens.

III.4. Comparison between *in situ* diffraction and EPSC modeling

The model gives access to the strain/stress state of each grain in the diffracting volume for a given macroscopic strain. It is possible to compare the experimental mechanical behavior at the diffracting volume scale, measured during *in situ* X-ray diffraction tensile experiments, to the simulated microscopic mechanical behavior. Varying the angles φ and ψ enables to probe different grain groups that have experienced a different deformation history depending on their orientation with respect to the tensile direction.

Predicted and experimental lattice strain pole figures for the {331} plane families are shown in Fig. 10 for 4 macroscopic strains (0.2, 0.5, 0.8 and 3 %). Let us first focus on the development of the *in situ* measured elastic lattice strains for the BD sample and on a particular orientation, for example (φ = 90°; ψ = 50°). The strain pole figures calculated with the EPSC model display the same features as the experimental results. The elastic domain is very well reproduced. For example, the measured (respectively predicted) lattice strain at 0.2 % macroscopic strain is 802 με (resp. 796 με). During the elastoplastic transition (0.5 % macroscopic strain), the simulated values deviate slightly from the experimental ones. The predicted strain is about 10 % larger than the measured value. Finally, at 3 % macroscopic strain, the difference reaches 6 %.

The discrepancies between measurements and model calculations are more pronounced perpendicularly to the tensile axis (φ = 0°; ψ = 0°). In the elastic domain, the predicted and experimental lattice strain are, respectively -520 με and -300 με. These differences decrease with increasing strain. During the elastoplastic transition, the simulation shows a deviation of about 20 % (i.e., about -1040 με) from the experiment (-855 με). At 3 % strain, the deviations are around 16 %. Different authors have already highlighted that these discrepancies between simulations and measurements are more pronounced perpendicularly to the loading axis [35–37].

For the WD and GD specimens, the predicted results reproduce well the behavior identified experimentally using XRD (Figure 10). In the tensile direction (φ = 90°; ψ = 50°), the simulated strains are very close to those determined with XRD but they remain systematically lower than 7 % whatever the applied strain for both WD and GD specimens. The elastic domain (0.2 % macroscopic strain) is also well reproduced: the measured (respectively predicted) lattice strains are: 847 με (resp. 803 με) for the WD specimen. It can be noted that the smallest discrepancies between model and experiment are about 3 % at 3 % macroscopic strain. The maximum deviation observed in the tensile direction (φ = 90°) is 7 % and is reached in the elastoplastic transition for both specimens (e.g. 1280 με for the simulated lattice strains against 1372 με for the measured lattice strain for the GD specimen).

In the direction perpendicular to the tensile axis (i.e. φ = 0°; ψ = 0°), higher discrepancies are observed. They do not exceed 16 % in any case. The largest discrepancies (14 % for the GD specimen and 16 % for the WD specimen) are observed during the elastoplastic transition. In elasticity, the deviations are smaller (less than 10 %) for both specimens. In the plastic domain, at 3 % macroscopic strain, the differences obtained are very weak (e.g. -1191 με for the simulated lattice strains against -1146 με for the measured lattice strains for the WD specimen). The model correctly describes the macroscopic mechanical behavior as well as the elastic strain field in the diffracting volume whatever the considered specimen. All the predicted values in elasticity are relatively close to the experimental ones, validating the choice made for the pure aluminum single-crystal elastic constants for the simulations.

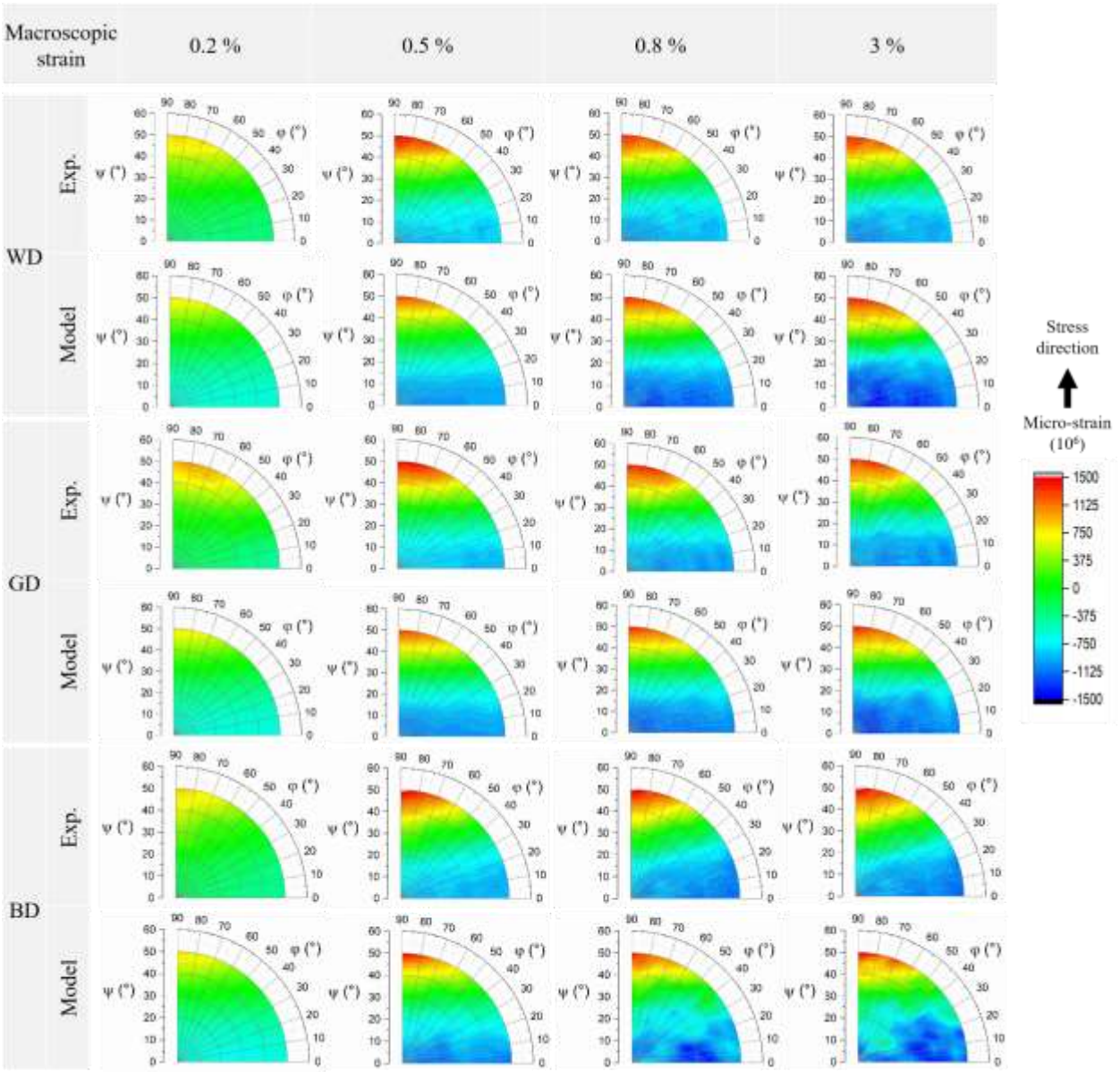

Figure 10: experimental and simulated lattice strain pole figures for WD, BD and GD specimens.

To explain the discrepancies between experimental results and simulation, some explanations can be proposed. More significant deviations of the simulated results from the experimental data can be observed in the direction perpendicular to the tensile axis To explain this point, it has to be noted that the grains which contribute to a given {hk.l} reflection in the loading direction involve only similarly oriented grains with respect to this direction and are thus not so sensitive to slight

variations in the representation of the crystallographic texture, contrary to {hk.l} grain groups in the direction perpendicular to the tensile axis. All grains with a plane-normal vector colinear to the scattering vector of the transverse direction, for a given {hk.l} reflection, have a shared (hk.l) plane-normal perpendicular to the loading axis. The grains which contribute to the reflection display many different crystallographic orientations with respect to the loading axis. In other words, a rotation of a grain around an axis perpendicular to the loading direction highly changes the stiffness in the tensile direction and, consequently, the strain and stress state in the grain. Different authors have already highlighted that these discrepancies between simulations and measurements are more pronounced perpendicularly to the loading axis [35–37]. The microscopic scale has not been explicitly described in the model (only one scale transition and the contribution of particles to single-crystal straining and hardening is not considered). In this study, the local behaviour (at the grain level) is based on the assumption of uniform mechanical fields. This approach permits to predict correctly the yield surface, the crystallographic texture linked to the plastic deformation, the intergranular stresses due to the initial and induced anisotropy during monotonic loading. To describe with more accuracy the metallurgical state at the grain level, a micro-mechanical description of a single crystal containing particles needs to be developed through a micro–meso transition. A modified Schmid's law and a new hardening matrix, taking into account the usual dislocation–dislocations interactions and also interactions between dislocations and particles, can be proposed. Next, a meso–macro transition using the self-consistent method proposed in the present work can be applied to deduce the global response of the polycrystalline material.

Conclusions

589 The mechanical properties of parts built by the WAAM process have been studied at the different
590 scales of the material. The findings from the current study can be summarized as follows:

591 • Tensile tests carried out on samples extracted from the WAAM walls along three different
592 orientations did not reveal relevant significant differences and thus demonstrate the quasi-
593 isotropic character of the mechanical properties of the built material. The presence of
594 equiaxed grains has probably reduced the anisotropic effect of columnar grains. Mechanical
595 properties of the deposited material are slightly better as compared to conventional rolled
596 material in T6 state.

597 • The residual stresses were characterized at the surface and in the bulk using diffraction.
598 Although the residual stress values are low on the close-surface (40 MPa for the maximum
599 value), the mechanical state is different in depth with significant maximum residual stress
600 levels (+/- 100 MPa).

601 • A coupled method using a mean field approach and *in situ* mechanical XRD tests has been
602 developed in order to better understand the development and the evolution of internal lattice
603 strains under mechanical loading, considering the main microstructural features. The EPSC
604 model enables to reproduce accurately the XRD strain pole figures as a function of the
605 applied macroscopic deformation for the three sampling directions.

606

607 **References**

608

609 [1] T. DebRoy, H.L. Wei, J.S. Zuback, T. Mukherjee, J.W. Elmer, J.O. Milewski, A.M. Beese,
610 A. Wilson-Heid, A. De, W. Zhang, Additive manufacturing of metallic components –
611 Process, structure and properties, Prog. Mater. Sci. 92 (2018) 112–224.

https://doi.org/10.1016/J.PMATSCI.2017.10.001.

[2] K.S. Derekar, A review of wire arc additive manufacturing and advances in wire arc additive manufacturing of aluminium, Mater. Sci. Technol. 34 (2018) 895–916. https://doi.org/10.1080/02670836.2018.1455012.

[3] X. Fang, L. Zhang, H. Li, C. Li, K. Huang, B. Lu, Microstructure Evolution and Mechanical Behavior of 2219 Aluminum Alloys Additively Fabricated by the Cold Metal Transfer Process, Materials (Basel). 11 (2018). https://doi.org/10.3390/ma11050812.

[4] C.R. Cunningham, S. Wikshåland, F. Xu, N. Kemakolam, A. Shokrani, V. Dhokia, S.T. Newman, Cost Modelling and Sensitivity Analysis of Wire and Arc Additive Manufacturing, Procedia Manuf. 11 (2017) 650–657. https://doi.org/10.1016/J.PROMFG.2017.07.163.

[5] Sindo Kou, Precipitation-Hardening Materials I: Aluminum Alloys, in: Weld. Metall., 2002: pp. 353–374. https://doi.org/https://doi.org/10.1002/0471434027.ch15.

[6] M.F.A. Ibrahim, S.R.S. Bakar, A. Jalar, N.K. Othman, J. Sharif, A.R. Daud, N.M. Rashdi, Effect of Porosity on Tensile Behaviour of Welded AA6061-T6 Aluminium Alloy, Appl. Mech. Mater. 66–68 (2011) 534–539. https://doi.org/10.4028/www.scientific.net/AMM.66-68.534.

[7] A. Elrefaey, Effectiveness of cold metal transfer process for welding 7075 aluminium alloys, Sci. Technol. Weld. Join. 20 (2015) 280–285. https://doi.org/10.1179/1362171815Y.0000000017.

[8] A. Benoit, P. Paillard, T. Baudin, J.-B. Mottin, Soudage homogène MIG de l'alliage d'aluminium 6061, MATEC Web Conf. 7 (2013). https://doi.org/10.1051/matecconf/20130702009.

[9] S. Selvi, A. Vishvaksenan, E. Rajasekar, Cold metal transfer (CMT) technology - An

636 overview, Def. Technol. 14 (2018) 28–44. https://doi.org/10.1016/J.DT.2017.08.002.
637 [10] G. Çam, G. İpekoğlu, Recent developments in joining of aluminum alloys, Int. J. Adv.
638 Manuf. Technol. 91 (2017) 1851–1866. https://doi.org/10.1007/s00170-016-9861-0.
639 [11] G. Doumenc, L. Couturier, B. Courant, P. Paillard, A. Benoit, E. Gautron, B. Girault, T.
640 Pirling, S. Cabeza, D. Gloaguen, Investigation of microstructure, hardness and residual
641 stresses of wire and arc additive manufactured 6061 aluminium alloy, Materialia. 25
642 (2022) 101520. https://doi.org/10.1016/J.MTLA.2022.101520.
643 [12] R. Acevedo, P. Sedlak, R. Kolman, M. Fredel, Residual stress analysis of additive
644 manufacturing of metallic parts using ultrasonic waves: State of the art review, J. Mater.
645 Res. Technol. 9 (2020) 9457–9477. https://doi.org/10.1016/J.JMRT.2020.05.092.
646 [13] F. Martina, M.J. Roy, B.A. Szost, S. Terzi, P.A. Colegrove, S.W. Williams, P.J. Withers, J.
647 Meyer, M. Hofmann, Residual stress of as-deposited and rolled wire+arc additive
648 manufacturing Ti–6Al–4V components, Mater. Sci. Technol. 32 (2016) 1439–1448.
649 https://doi.org/10.1080/02670836.2016.1142704.
650 [14] B.A. Szost, S. Terzi, F. Martina, D. Boisselier, A. Prytuliak, T. Pirling, M. Hofmann, D.J.
651 Jarvis, A comparative study of additive manufacturing techniques: Residual stress and
652 microstructural analysis of CLAD and WAAM printed Ti–6Al–4V components, Mater.
653 Des. 89 (2016) 559–567. https://doi.org/10.1016/J.MATDES.2015.09.115.
654 [15] K. Oyama, S. Diplas, M. M'hamdi, A.E. Gunnæs, A.S. Azar, Heat source management in
655 wire-arc additive manufacturing process for Al-Mg and Al-Si alloys, Addit. Manuf. 26
656 (2019) 180–192. https://doi.org/10.1016/J.ADDMA.2019.01.007.
657 [16] P. Rodríguez-González, E.M. Ruiz-Navas, E. Gordo, Wire Arc Additive Manufacturing
658 (WAAM) for Aluminum-Lithium Alloys: A Review, Materials (Basel). 16 (2023).
659 https://doi.org/10.3390/ma16041375.

[17] B. Wu, Z. Pan, D. Ding, D. Cuiuri, H. Li, J. Xu, J. Norrish, A review of the wire arc additive manufacturing of metals: properties, defects and quality improvement, J. Manuf. Process. 35 (2018) 127–139. https://doi.org/10.1016/J.JMAPRO.2018.08.001.

[18] V. Hauk, H. Behnken, Structural and Residual Stress Analysis by Nondestructive Methods, Transferre, Elsevier, Amsterdam, 1997. https://doi.org/10.1016/b978-0-444-82476-9.50022-0.

[19] M. François, B. Dionnet, J.M. Sprauel, F. Nardou, The Influence of Cylindrical Geometry on X-ray Stress Tensor Analysis. I. General Formulation, J. Appl. Crystallogr. 28 (1995) 761–767. https://doi.org/10.1107/S0021889895006868.

[20] T. Pirling, G. Bruno, P.J. Withers, SALSA—A new instrument for strain imaging in engineering materials and components, Mater. Sci. Eng. A. 437 (2006) 139–144. https://doi.org/10.1016/J.MSEA.2006.04.083.

[21] D. Richard, M. Ferrand, G.J. Kearley, Analysis and Visualisation of Neutron-Scattering Data, J. Neutron Res. 4 (1996) 33–39. https://doi.org/10.1080/10238169608200065.

[22] D. Gloaguen, B. Girault, B. Courant, P.A. Dubos, M.J. Moya, F. Edy, J. Rebelo Kornmeier, Study of Residual Stresses in Additively Manufactured Ti-6Al-4V by Neutron Diffraction Measurements, Metall. Mater. Trans. A Phys. Metall. Mater. Sci. 51 (2020) 951–961. https://doi.org/10.1007/s11661-019-05538-w.

[23] P.J. Withers, M. Preuss, A. Steuwer, J.W.L. Pang, Methods for obtaining the strain-free lattice parameter when using diffraction to determine residual stress, J. Appl. Crystallogr. 40 (2007) 891–904. https://doi.org/10.1107/S0021889807030269.

[24] M.A. Iadicola, T.H. Gnäupel-Herold, Effective X-ray elastic constant measurement for in situ stress measurement of biaxially strained AA5754-O, Mater. Sci. Eng. A. 545 (2012) 168–175. https://doi.org/10.1016/J.MSEA.2012.02.100.

[25] C. Gault, A. Dauger, P. Boch, Variations of the elastic constants of aluminium–magnesium single crystals with guinier-preston zones, Phys. Status Solidi. 43 (1977) 625–632. https://doi.org/https://doi.org/10.1002/pssa.2210430233.

[26] M. Lundberg, J. Saarimäki, J.J. Moverare, R.L. Peng, Effective X-ray elastic constant of cast iron, J. Mater. Sci. 53 (2018) 2766–2773. https://doi.org/10.1007/s10853-017-1657-6.

[27] D. Gloaguen, T. Berchi, E. Girard, R. Guillén, Measurement and prediction of residual stresses and crystallographic texture development in rolled Zircaloy-4 plates: X-ray diffraction and the self-consistent model, Acta Mater. 55 (2007) 4369–4379. https://doi.org/10.1016/J.ACTAMAT.2007.04.007.

[28] U.F. Kocks, Texture and anisotropy : preferred orientations in polycrystals and their effect on materials properties / U.F. Kocks, C.N. Tomé, H.-R. Wenk, authors and editors , Cambridge, U.K. , 1998.

[29] P. Franciosi, M. Berveiller, A. Zaoui, Latent hardening in copper and aluminium single crystals, Acta Metall. 28 (1980) 273–283. https://doi.org/10.1016/0001-6160(80)90162-5.

[30] A.C. Vermeulen, An elastic constants database and XEC calculator for use in XRD residual stress analysis, Adv. X-Ray Anal. 44 (2001) 128–133.

[31] P.S. Prevéy, X-Ray Diffraction Residual Stress Techniques, Mater. Charact. (1986) 380–392. https://doi.org/10.31399/asm.hb.v10.a0001761.

[32] J.R. Hönnige, P.A. Colegrove, S. Ganguly, E. Eimer, S. Kabra, S. Williams, Control of residual stress and distortion in aluminium wire + arc additive manufacture with rolling, Addit. Manuf. 22 (2018) 775–783. https://doi.org/10.1016/J.ADDMA.2018.06.015.

[33] B. Xie, J. Xue, X. Ren, W. Wu, Z. Lin, A Comparative Study of the CMT+P Process on 316L Stainless Steel Additive Manufacturing, Appl. Sci. 10 (2020). https://doi.org/10.3390/app10093284.

[34] P. Mercelis, J. Kruth, Residual stresses in selective laser sintering and selective laser melting, Rapid Prototyp. J. 12 (2006) 254–265. https://doi.org/10.1108/13552540610707013.

[35] C.J. Neil, J.A. Wollmershauser, B. Clausen, C.N. Tomé, S.R. Agnew, Modeling lattice strain evolution at finite strains and experimental verification for copper and stainless steel using in situ neutron diffraction, Int. J. Plast. 26 (2010) 1772–1791. https://doi.org/10.1016/J.IJPLAS.2010.03.005.

[36] O. Muránsky, D.G. Carr, M.R. Barnett, E.C. Oliver, P. Šittner, Investigation of deformation mechanisms involved in the plasticity of AZ31 Mg alloy: In situ neutron diffraction and EPSC modelling, Mater. Sci. Eng. A. 496 (2008) 14–24. https://doi.org/10.1016/j.msea.2008.07.031.

[37] D. Gloaguen, G. Oum, V. Legrand, J. Fajoui, M.J. Moya, T. Pirling, W. Kockelmann, Intergranular Strain Evolution in Titanium During Tensile Loading: Neutron Diffraction and Polycrystalline Model, Metall. Mater. Trans. A Phys. Metall. Mater. Sci. 46 (2015) 5038–5046. https://doi.org/10.1007/s11661-015-3073-3.